Numerical and experimental investigation of the effect of geometry modification on the aerodynamic characteristics of a NACA 64(2)-415 wing

P R A D E E P R A M E S H

Master of Science Thesis
Stockholm, Sweden 2013

Numerical and experimental investigation of the effect of geometry modification on the aerodynamic characteristics of a NACA 64(2)-415 wing

P R A D E E P R A M E S H

Master's Thesis in Scientific Computing (30 ECTS credits)
Master Programme in Scientific Computing 120 credits
Royal Institute of Technology year 2013
Supervisor at KTH was Johan Jansson
Examiner was Michael Hanke

TRITA-MAT-E 2013:11
ISRN-KTH/MAT/E--13/11--SE

Royal Institute of Technology
School of Engineering Sciences

KTH SCI
SE-100 44 Stockholm, Sweden

URL: www.kth.se/sci

Abstract

The objective of the thesis is to study the effect of geometry modifications on the aerodynamic characteristics of a standard airfoil (NACA series). The airfoil was chosen for a high aspect ratio and Reynolds number of the range $10^6 - 10^7$ (realistic conditions for flight and naval applications). Experimental and Numerical investigation were executed in collaboration with KTH – CTL and Schlumberger. Experimental investigations were conducted at NTNU which was funded by Schlumberger. The numerical investigation was executed with the massively parallel unified continuum adaptive finite element method solver "Unicorn" and the computing resources at KTH – CTL. The numerical results are validated against the experiments and against experimental results in the literature, and possible discrepancies analyzed and discussed based on the numerical method. In addition, this will help us to expand our horizon and get acquainted with the numerical methods and the computational framework. The further scope of this thesis is to develop and implement the new modules for the Unicorn solver suitable for the aerodynamic applications.

Numerisk och experimentell undersökning av effekten av geometrimodifikationer på NACA-profil på dess aerodynamiska egenskaper.

Sammanfattning

I arbetet studeras effekten av geometri-modifikationer på aerodynamiska egenskaper hos en standard-vingprofil ur NACA-serien. Profilen valdes för en slank vinge och Reynoldstal mellan en och tio miljoner vilket kan vara realistiskt för flygplan och marina tillämpningar. Experiment och numeriska beräkningar utförs i samarbete mellan KTH/CTL och Schlumberger. Experimenten utfördes på NTNU med stöd av Schlumberger. Beräkningarna gjordes med finita-element paketet "Unicorn" på KTH/CTL s datorer. Nya Unicorn-moduler för aerodynamiska beräkningar utvecklas vilket ger erfarenhet av de numeriska metoderna och beräkningsmiljön. Numeriska resultat valideras mot experimenten och resultat i litteraturen, och avvikelserna för den aktuella numeriska metoden analyseras.

Acknowledgement

I would like to express my sincere gratitude to my supervisor Johan Jansson, for his continuous guidance and support in all stages of the thesis. He provided me with direction, technical support and became more of a mentor and friend, than a professor.I appreciate and would also like to thank him for being an open person to ideas, for encouraging and helping me to shape my interest and ideas.

A very special thanks to Martin Howlid, Nils Halvor Heieren and Rik Wemmenhove from Schlumberger-WOTC, Norway for the support and assistance they provided at all levels of the project. I recognize that this research would not have been possible without financial support from Schlumberger-WOTC for the Wind Tunnel Experiments.

I would like to thank Per-Åge Krogstad and Tania Bracchi from the department of energy and process engineering at NTNU, who were involved in this project for conducting the experiments at the Aerodynamic Laboratory.

I would like to thank Johan Hoffman for the valuable inputs, support and computational resources from Computational Technology Laboratory @ KTH. In addition, I would like to thank Michael Hanke for the administrative support and guidance.

Pradeep Ramesh

Table of Contents

List of Abbreviations

NACA	National Advisory Committee for Aeronautics
AOA	Angle of Attack
DNS	Direct Numerical Simulation
RANS	Reynolds-averaged Navier-Stokes
LES	Large Eddy Simulations
ILES	Implicit Large Eddy Simulations
DES	Detached Eddy Simulations
FEM	Finite Element Method
CFD	Computational Fluid Dynamics
3D	Three Dimensional

1. Introduction

The prime motivation for this project was realistic problems that occur in field operation at the Schlumberger company. The main focus is to investigate and observe, how damages contribute in performance of a wing and how to resolve these field problems. After numerous meetings and discussions the project idea was formulated in collaboration with Schlumberger.

Numerical simulations were computed for 3D Unsteady, Incompressbile turbulent flow past a NACA 64(2)415 wing for chord length $c = 242\ mm\ and\ aspect\ ratio = 5$ for a range of angles of attack from low lift through stall. Two variants were considered for the investigation , case I - clean wing and case – II protrusion wing. The numerical investigation was executed with the massively parallel unified continuum adaptive finite element method solver “Unicorn” . A stabilized finite element method is used, referred to as General Galerkin (G2), with adaptive mesh refinement with respect to the error in target output, such as aerodynamic forces.

Experimental investigations have been carried out at NTNU wind tunnel laboratory in collaboration with schlumberger. Computational predictions of aerodynamic characteristics are validated against experimental data.

2. Project Background

State of Art:

Today, a major computational challenge is to compute aerodynamic forces and predict stall accurately and efficiently at realistic flight conditions [1].

In the current scenario most of the simulations in the aircraft industry are based on Reynolds averaged Navier- Stokes equations (RANS), where time averages are computed to an affordable cost, with the drawback of introducing turbulence models based on parameters that have to be tuned for particular applications. Large eddy simulation (LES) [3] is an alternative over Direct Numerical Simulations (DNS) and RANS.

An adaptive finite element method, the General Galerkin (G2) method [4] is adopted in our simulation method. In G2 method the residual based numerical stabilization acts as a subgrid model similar to an Implicit LES (ILES) [3]. An adaptive mesh refinement algorithm is used, driven by a posteriori estimation of the error,chosen as the target output based on the solution of an dual problem.

According to *Johan Hoffman , Johan Jansson, and Niclas Jansson [13] "*A key challenge for LES methods is the modeling of turbulent boundary layers at different angles of attack. Full resolution of turbulent boundary layers is not feasible, due to the high cost associated with computational representation of all the physical scales. Instead cheaper models are used, including resolution of the boundary layer only in the wall-normal direction, wall shear stress models, and hybrid LES-RANS models such as DES [13–17]. For high reynolds numbers, a slip with friction boundary condition is used [4], corresponding to a simple wall shear stress model of the type proposed by Schumann [18]".

We consider zero skin friction, corresponding to a free slip boundary condition, an approach that previously has been used in [10–12].

Working Principle:

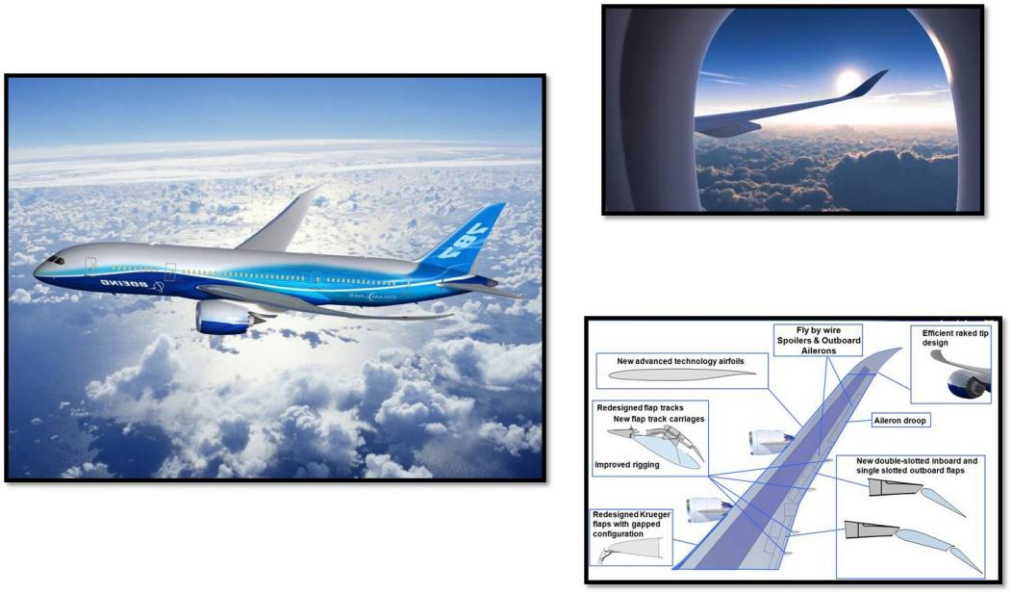

Figure 1: Overview of the Wing

The wing of an aircraft is one of the critical part in aerodynamics. The wings are attached to each side of the fuselage and are the main lifting surfaces that support the airplane in flight.

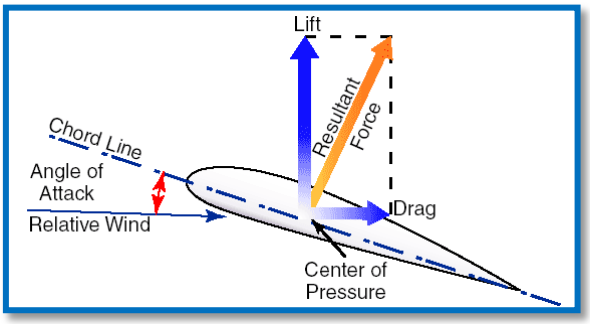

Figure 2 : Working Principle of a Wing

The fluid flow over and under the wing surfaces travels at different velocities producing a difference in air pressure low above the wing and high below it. The four forces acting on the airplane during the flight condition are – LIFT, DRAG, THRUST, WEIGHT.

- LIFT is the component of aerodynamic force perpendicular to the relative wind.
- DRAG is the component of aerodynamic force parallel to the relative wind.
- THRUST is the force produced by the engine. It is directed forward along the axis of the engine.
- WEIGHT is the force directed downward from the center of mass of the airplane towards the center of the earth.

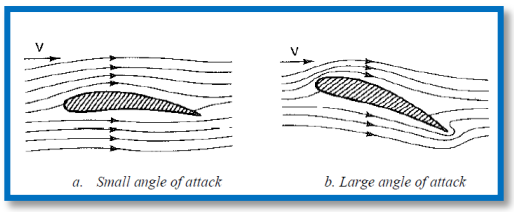

Figure 3 : Flow around an Airfoil

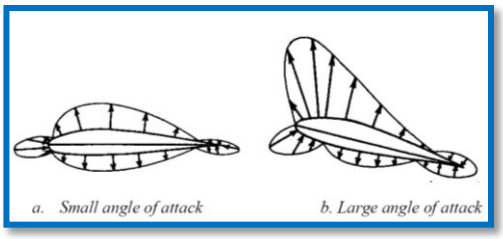

Figure 4 : Pressure Distribution around an Airfoil

The low pressure exerts a pulling force and the high pressure a pushing force. The lifting force usually called lift, depends on the shape, area, the angle of attact and on the speed of the aircraft. The shape of the wing causes the air streaming above and below the wing to travel at different velocities. According to Bernoulli's principle, it is this difference in air velocity that produces the difference in air pressure.

In aerodynamics, the lift-to-drag ratio, or L/D ratio, is the amount of lift generated by an airfoil, divided by the drag it creates by moving through the air. An airplane has a high L/D ratio if it produces a large amount of lift or a small amount of drag. A higher or more favourable L/D ratio is typically one of the major goals in aircraft design.

$$Ratio = \frac{Lift}{Drag} = \frac{L}{D}$$

For the gliding flight of birds and airplanes with fixed wings, L/D ratio is typically between 10 and 20,

$$10 < \frac{L}{D} > 20$$

Aerodynamic Forces and Coefficients

The force acting on the wing, perpendicular to the direction of the flow is defined as a lift force (L). The force acting on the wing, parallel to the direction of the flow is defined as a drag force (D). The Lift and drag coefficient, thus represent global mean values in space-time. The forces depend on number of geometric and flow parameters. Its is advantageous to work with nondimensionalized forces and moments for which most of these parameters dependencies are scaled out.

The nondimensional force coefficients are given by:

Lift coefficient : $$C_L = \frac{L}{q_\infty A}$$

Drag coefficient : $$C_D = \frac{D}{q_\infty A}$$

Where,

Lift force : L

Drag force : D

Planform : $A = Chord * Span$

Fluid Velocity : U_∞

Dynamic pressure : $q_\infty = \frac{1}{2}\rho U_\infty^2$

Dimensional analysis reveals that the nondimensional coefficients depends on the angle of attack α, the Reynolds number Re , the Mach number M_∞ and on the airfoil shape.

$$C_L , C_D = f(\alpha , Re , M_\infty , Airfoil\ shape)$$

For low speeds flows, M_∞ has virtually no effect and for a given airfoil shape, we have :

$$\boldsymbol{C_L , C_D = f(\alpha , Re)}$$

Airfoil Characteritics:

The fundamental parameters of airfoil characteristics are :

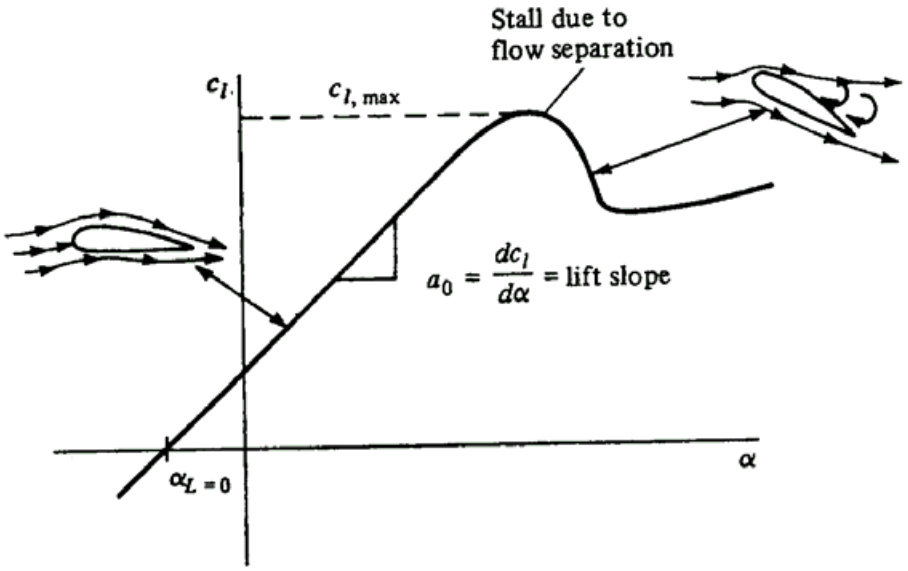

Figure 5 : Airofoil Characteristics

1. **Angle of Attack** [α] **:** α is the angle between the free-stream velocity and the chord.
2. **Aspect Ratio**$[AR]$**:** Aspect ratio is the ratio between the span of an airfoil and its chord.

$$AR = \frac{Span\ (m)}{Chord(m)}$$

Wings with larger aspect ratios generate higher lift with less drag and thus have greater flight efficiency. A high aspect ratio wing is efficient because it reduces the formation of the vortex and associated drag.

3. **Stall:** The pressure distribution on the surface of the airfoil is dependent on the angle of attack. The higher the angle, the greater is the perturbation to the flow, causing higher velocities and lower pressures over the upper surface. At higher angles of attack, the adverse pressure gradient become too high, causing the flow to separate from the surface of the airfoil. As the angle of attack is increased, lift is also increased up to a certain angle. Beyond this angle airflow can no longer follow the contour of the airfoil's upper surface . The region of flow right next to the upper surface induces reverse flow and the pressure distribution over the upper surface causing a sudden loss of the lifting force. This phenomenon is termed as “Stall”. The Stall angle is the angle at which the flow separation occurs.

Finite Element Method (FEM)

The finite element method (FEM) is a computational technique used to obtain approximate solutions of boundary value problems in engineering. FEM is used for problems with complicated geometries, loadings, and material properties where analytical solutions cannot be obtained.

Figure 6 : Idea of FEM

Basic laws of nature are typically expressed in the form of partial differential equations (PDE), such as Navier-Stokes equations of fluid flow. The Finite element method has emerged as a universal tool for the computational solution of PDEs with a multitude of applications in engineering and science. Adaptivity is an important computational technology where the FEM algorithm is automatically tailored to compute a user specified output of interest to a chosen accuracy, to a minimal computational cost.

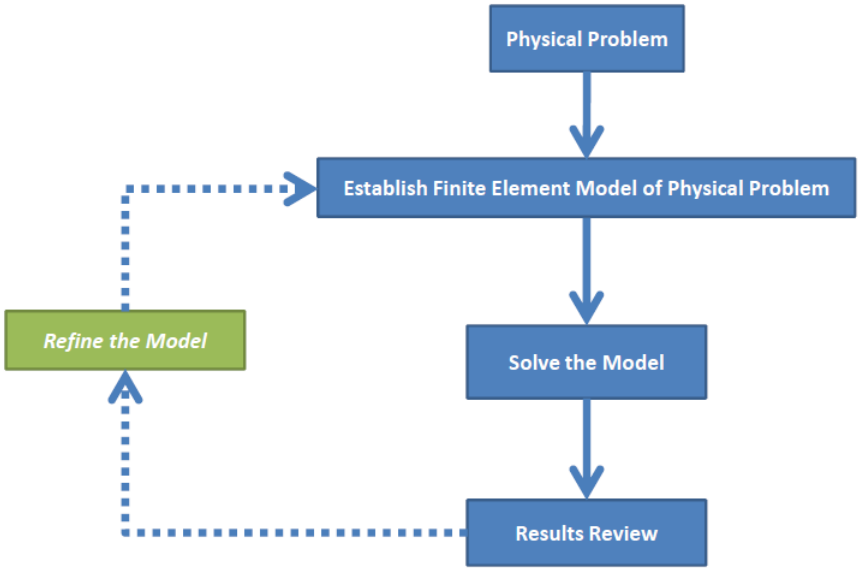

Figure 7 : Finite Element Process

In the Finite Element Method (FEM) we approximate the exact solution function "u" as a piecewise polynomial and compute co-efficients by enforcing orthogonality (Galerkin's Method) [13] [14] [15].

The basic steps involved in FEM are explained as below [18] :

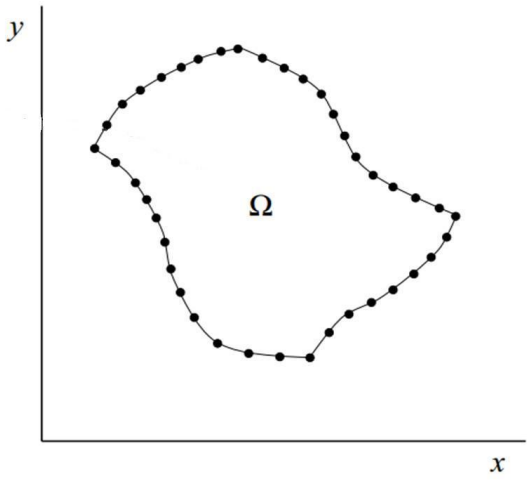

Figure 8 : Finite Element Domain

Polynomial Approximation:

We seek polynomial approximations "U" to "u". A vector space can be constructed with a set of polynomials on a domain (Ω) as basis vectors, where function addition and scalar multiplication satisfy the requirements for a vector space.

We can also define an inner product space with the $\boldsymbol{L_2}$ inner product defined as:

$$(f, g)_{L_2} = \int_{\Omega} f(x)\, g(x)\, dx$$

The $\boldsymbol{L_2}$ inner product generates the $\boldsymbol{L_2}$ norm:

$$\|f\|_{L_2} = \sqrt{(f, f)_{L_2}}$$

Just like in $\boldsymbol{R^d}$ we define orthogonality between two vectors as :

$$(f, g)_{L_2} = 0$$

The Cauchy-Schwartz inequality is given by:

$$\left|(f,g)_{L_2}\right| \leq \|f\|_{L_2}\|g\|_{L_2}$$

Polynomial vector space $V^q = P^q(a,b)$ consists of polynomials:

$$p(x) = \sum_{i=0}^{q} c_i x^i$$

One basis is the monomials: $\{1, x, \ldots. , x^q\}$

Piecewise linear polynomials:

Global polynomials on the whole domain (a,b) led to vector space V^q (monomials basis: $\{1, x, \ldots. , x^q\}$). Only way of refining approximate solution U is by increasing q . We instead look at piecewise polynomials.

Partition domain $I = (a,b)$ into mesh: $a = x_0 < x_1 < x_2 < \cdots < x_{m+1} = b$ by placing nodes x_i. We define polynomial function on each subinterval $I_i = (x_{i-1}, x_i)$ with length $h_i = x_i - x_{i-1}$

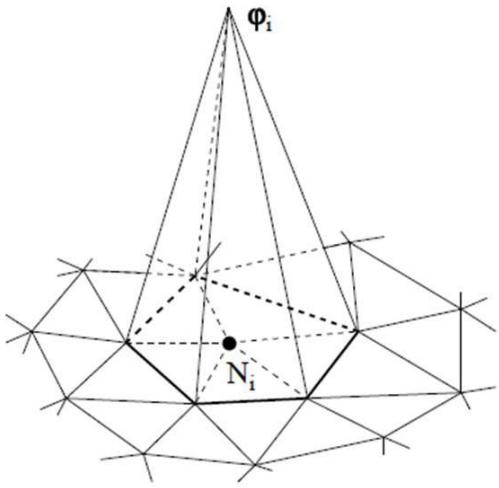

Figure 9 : Global basis "tent" function

Nodal Basis: $\emptyset_i(x_i) = 1,\ \emptyset_i(x_j) = 0,\ i \neq j$

Basis function: $\emptyset_i(x)$:

$$\emptyset_i(x) = \begin{cases} 0, & x \notin [x_{i-1},\ x_{i+1}], \\ \dfrac{x - x_{i-1}}{x_i - x_{i-1}}, & x \in [x_{i-1},\ x_i], \\ \dfrac{x - x_{i+1}}{x_i - x_{i+1}}, & x \in [x_i,\ x_{i+1}]. \end{cases}$$

Vector Space of continuous piecewise linear polynomials: V_h with basis $\{\emptyset_i\}_1^M$, M number of nodes in mesh.

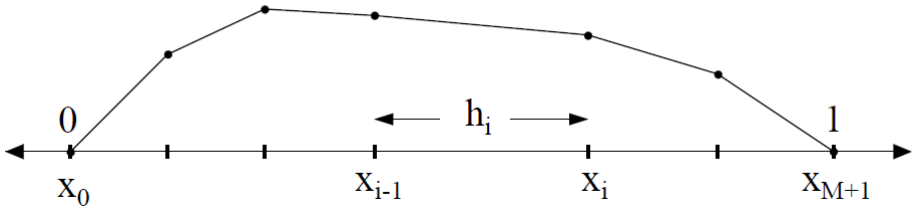

Figure 10 : Piecewise linear polynomials

Piecewise linear function:

$$U(x) = \sum_{j=1}^{M} \xi_j\ \emptyset_j(x)$$

We define the residual function $R(U)$ for a differential equation $A(u) = f$ as :

$$R(U) = A(U) - f, \qquad x \in I_i$$

We can thus define an equation with exact solution u as:

$$R(u) = 0$$

Galerkin's method:

We seek a solution U in finite element vector space V_h of the form:

$$U(x) = \sum_{j=1}^{M} \xi_j \ \emptyset_j(x)$$

We require the residual to be orthogonal to V_h :

$$(R(U), v) = \ 0, \forall \ v \ \in \ V_h$$

This form is also known as the "Weak formulation".

For terms in $R(u)$ with two derivatives we perform integration by parts to move one derivative to the test function.

In a nutshell the *Mathematical Model Formulation for our case is described as below:*

Method – PDE

For a given differential equation,

$$R(u) = 0$$

Function Space V and Discrete function Space, V_h

Weak form of the PDE is given by:

$$(R(u), v) = 0, \qquad \forall \ v \ \in V, u \ \in V$$

Numerical Approximation

The Finite Element Method is defined by:

$$(R(U), v) = 0, \qquad \forall \ v \ \in V_h$$

Where Discrete Space, $V_h = \ \{\phi_i\}_0^M$

$$U = \sum_{i=0}^{M} \xi_i \, \phi_i \ , \qquad U \in V_h$$

Numerical Approximation applied to Fluid flow

$$R(U) = Navier\ Stokes\ Eq. + Stabilization\ Terms$$

Refer Eq. (i) in page no.23 and Eq. (ii) in page no.27

Error Estimation

We follow the general framework for a posteriori error estimation based on the solution of associated dual problems.

We use an A Posteriori Error Estimate , where e is the error and Ψ is an output functional of interest.

$$e = u - U$$

$$|(e, \Psi)| \leq TOL$$

$$(e, \Psi) = \int_{\Omega} e \, . \Psi \, \mathrm{dx}$$

Residual:

$$R(U) = AU - f$$

Primal Problem: $AU = f$

Dual Problem: $A^* \phi = \Psi$

A Posteriori Error Estimate can be re-written as:

$$|(e, \Psi)| = |(-R(u), \phi)|$$

Further estimates (see [4]) results in the following Error Indicator:

$$\varepsilon_k = h_k \|R(U)\|_k \, \|D\phi\|_k$$

Adaptive Algorithm

In practice, the dual solution is approximated by a similar finite element method as we use for the primal problem, linearized at the primal solution. Based on the a posteriori error indicator we can then form adaptive algorithms for how to construct finite element meshes optimized to approximate the functional.

Starting from an initial coarse mesh $\mathcal{T}^0$, one simple such algorithm implemented in Unicorn takes the form: let k = 0 then do :

Adaptive mesh refinement Algorithm

1. For the mesh $\mathcal{T}^k$ compute the primal problem and the dual problem.
2. If $\sum_{k\in\mathcal{T}^k} \varepsilon_k < TOL$ then stop, else:
3. Mark some chosen percentage of the elements with highest ε_k for refinement
4. Generate the refined mesh $\mathcal{T}^{k+1}$, set k = k+1, and go to 1.

3. NACA Airfoil

During the initial stage of our project, we had to choose a wing suitable for project specifications. A wing having high aspect ratio (HR = 5), Reynolds number of range (Re) 10^6 – 10^7, published data and geometry modifications are permitted. NTNU had two wings prototypes at their inventory. Considering our project specifications, NTNU proposed two wing prototypes:

1. "Stratford" wing, developed at NTNU and Confidential (Re= ~ 0.8M). As it was a custom wing developed at NTNU, we were not allowed to do any geometry modifications.
2. "NACA64 (2)-415" wing - high aspect ratio standard wing (Re= ~ 0.5M). We were allowed to make the geometry modifications.

The specifications of the NACA wing were in-line with our project specifications. Based on the cost estimation, time limitations and the specifications, we decided to use the "NACA64 (2)-415 wing", for our project.

Nomenclature

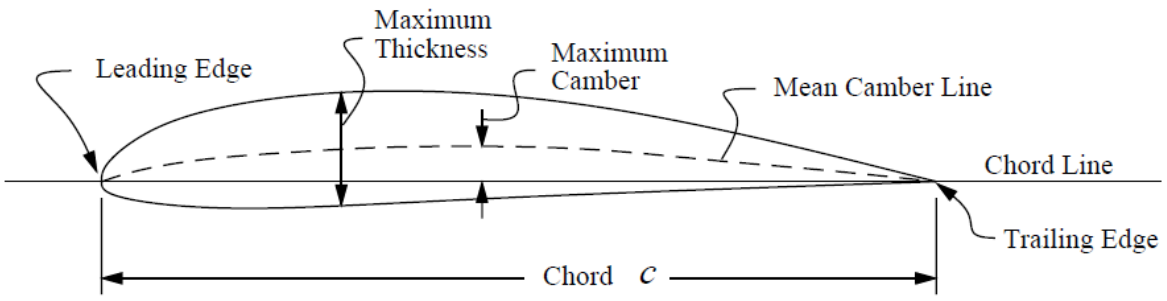

Figure 11 : Cambered Airfoil Geometry

The figure above shows the key terms used in nomenclature of the Airfoil Geometry. The mean camber line is defined to lie halfway between the upper and lower surface

$NACA\ 64_2 - 415$

Where,

- "$NACA$" stands for National Advisory Committee for Aeronautics
- "6" denotes the Series designation
- "4" denotes the chordwise position of minimum pressure in tenths of the chord behind the leading edge for the basic symmetrical section at zero lift
- The subscript "2" indicates the range of lift coefficient in tenths above and below the design lift coefficient in which favourable pressure gradient exist on both surfaces
- "4" following the dash denotes the design lift coefficient in tenths
- The final two digits "15" denotes airfoil thickness in percent of the chord (15%)

The Cambered airfoil sections of all NACA families considered herein are obtained by combining a mean line and a thickness distribution [16] [17].

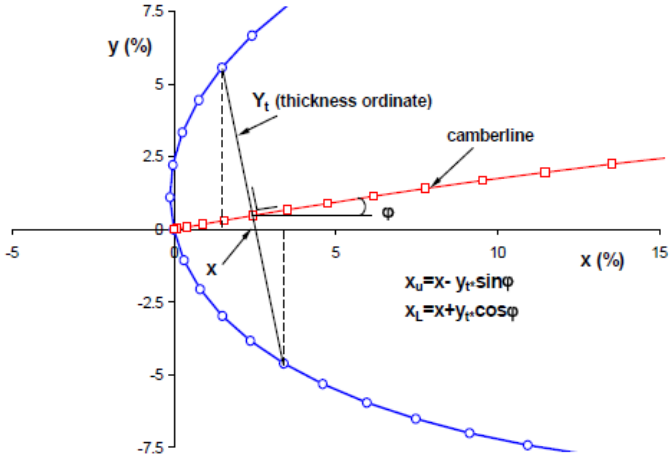

Figure 12 : NACA Airfoil co-ordinates

The abscissas, ordinates and slopes of the mean line are designated as x_c , y_c and $\tan\theta$ respectively. If x_u and y_u represent the abscissa and ordinate of a typical point of the Upper surface of the airfoil and y_t is the ordinate of the symmetrical thickness distribution

at the Chordwise position x , the upper surface coordinates are given be the following relations:

$$x_u = x - y_t(x)\ \sin\theta$$

$$y_u = y_c(x) + y_t(x)\ \cos\theta$$

The Corresponding expressions for the lower surface coordinates are:

$$x_l = x + y_t(x)\ \sin\theta$$

$$y_l = y_c(x) - y_t(x)\ \cos\theta$$

Where $y_t(x)$ is the thickness function

$y_c(x)$ is the camber line function and

$\theta = \tan^{-1}\left(\frac{dy_c}{dx}\right)$ is the camber line slope

4. Numerical Investigation

4.1. Governing Equations

In fluid mechanics, flow of air at subsonic speed is captured by the incompressible navier-stokes equations with the Reynolds number (Re) as an important flow characteristic,

$$Re = \frac{U\,L}{v}$$

Where: U is a characteristic flow speed

L is a characteristic length scale

v is the kinematic viscosity [For water $v \approx 10^{-6}$ and for air $v \approx 10^{-5}$]

The basic mathematical model for a flight simulation consists of Navier-Stokes equations expressing conservation of mass, momentum and energy of a viscous fluid. The incompressible Navier-Stokes equations thus can be viewed to consist of two equations in the fluid velocity and pressure expressing

- Newton's 2nd Law (conservation of momentum)
- Incompressibility.

As a basic model we use the Incompressible Navier-Stokes Equations for Velocity and Pressure:

$$\partial_t u + (u \cdot \nabla)u + \nabla p = g + \frac{1}{Re} \cdot \Delta u \qquad \text{..... (i)}$$

$$\nabla \cdot u = 0$$

$$\hat{u}(\cdot\ ,0) = \hat{u}^0$$

with $\vartheta = \mu/\rho_0$ the kinematic viscosity.

NOTE: Flight at speeds up to 300 km/h (83.33 m/s) of airplanes is described by solutions of the incompressible Navier-Stokes equations at a Reynolds number of size 10^6 or larger, which with normalization to $U = L = 1$ translate to small viscosity of size 10^{-6} or smaller. Typically for flows with Mach number below 0.2 - 0.3 can be modeled as incompressible

4.2. Computing Lift and Drag Coefficients

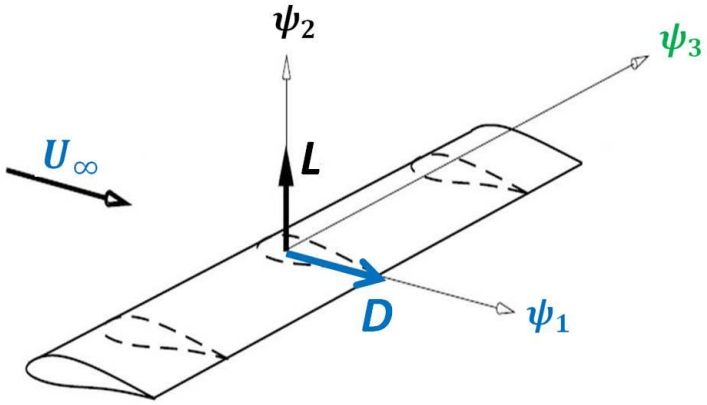

Figure 13 : 3D wing with directions

We consider a 3D wing with a surface Γ_0 placed in a horizontal channel and surrounded by a fluid flow $\hat{u} = (u, p)$ which we assume is satisfying the navier stokes equations. The mean value in time over a time interval $I = [0, \hat{t}]$ of the fluid force acting on the body surface in a direction $\psi = (\psi_1, \psi_2, \psi_3)$ is given by:

$$N(\sigma(\hat{u})) = \frac{1}{|I|}\int_I \int_{\Gamma_0} \sum_{i,j=1}^{3} \sigma_{ij}(\hat{u})\, n_j\, \psi_i ds\, dt$$

Where $\sigma(\hat{u})$ is the stress on Γ_0 given by $\hat{u}$. If ψ is directed along the channel in the direction of the flow, then $N(\sigma(\hat{u}))$ is a mean value in time of the drag force. If ψ is directed upwards, then $N(\sigma(\hat{u}))$ is a mean value in time of the lift force. The drag and lift co-efficients are normalised versions of $N(\sigma(\hat{u}))$.

With the computed the mean values of Lift and Drag forces we can calculate the normalised mean values Lift and Drag coefficients:

If the force is acting in the ψ_1 direction, we have $Drag\ force = N(\sigma(\hat{u}))$,

$$C_D = \frac{N(\sigma(\hat{u}))}{\frac{1}{2}U^2 A}$$

If the force is acting in the ψ_2 direction, we have $Lift\ force = N(\sigma(\hat{u}))$,

$$C_L = \frac{N(\sigma(\hat{u}))}{\frac{1}{2}U^2 A}$$

4.2. Boundary Conditions for the Numerical Method

The Navier-Stokes equations in the fluid domain are complemented by *boundary conditions* on the boundary of the fluid domain prescribing velocities or forces or combinations. We will be considering the "Slip" normal velocity and tangential forces are put to zero. [13]

We model the turbulent boundary layer by a slip with friction boundary condition which can be written:

$$u \cdot n = 0$$

$$u \cdot T_k + \beta^{-1} n^T \sigma \, T_k = 0, \;\; k = 1,2,$$

$$(u \cdot T_k) \, \beta + n^T \sigma \, T_k = 0,$$

with n an outward unit normal vector, and T_k orthogonal unit tangent vectors at the boundary. Here β can be chosen as a constant parameter, or as a function of space and time, similar to simple wall shear stress models. For very high Reynolds numbers we find that $\beta = 0$ is a good approximation for small skin friction stress, which have been validated for a number of benchmark problems [13] .

According to *Johan Hoffman, Johan Jansson, Niclas Jansson [13]* "The slip boundary condition is implemented in strong form, where the boundary condition is applied after assembling the left-hand side matrix and the right-hand side vector modifying the algebraic system, whereas the tangential components are implemented in weak form by adding boundary integrals in the variational formulation.

The node normals are computed from a weighted average of the surrounding facet normals. Edges and corners are identified from the angles between facet normals, for which the velocity is constrained in 2 and 3 linearly independent directions respectively".

We need to be careful when constucting the mesh near rounded surfaces of sharp radius, to avoid artificially constraining velocities.

4.3. Description of the Numerical Method

Continiuing from the desription of the FEM section in the background, we now choose a specific residual with stabalization as described below : ***General Galerkin (G2) Method***

General Galerkin ”G2” is a new computational method for turbulent flow, where a stabilized Galerkin finite element method is used to compute approximate weak solutions to the Navier-Stokes equations directly, without any filtering of the equations as in a standard approach to turbulence simulation. G2 is based on a posteriori error estimates, where the output sensitivity information is obtained by computational approximation of an associated dual problem, linearized at an approximate G2 solution $\widehat{U}$, with data coupling to the output of interest. The G2 method for high Reynolds number flow, including turbulent flow and shocks, takes the form of a standard Galerkin finite element discretization together with residual based numerical stabilization. [13]

We split the time interval I into sub intervals $I_n = (t_{n-1}, t_n)$, with associated space-time slabs $S_n = \Omega \times I_n$, over which we define space-time finite element spaces, based on a spatial finite element space V_h defined for a spatial mesh T_n .

In a $cG(1)cG(1)$ method, we seek an approximate solution $\widehat{U} = (U, P)$ which is continuous piecewise linear in space and time. With V_h a standard finite element space of continuous piecewise linear functions which is zero on the boundary Γ, the $cG(1)cG(1)$ method for constant density incompressible flow with homogeneous Dirichlet boundary conditions for the velocity takes the form:

for $n = 1, \dots, N$

Find $(U^n, P^n) \equiv \big(U(t_n), P(t_n)\big)$ with $U^n \in V_0^n \equiv [V_h^0]^3$ and $P^n \in V_h$,
Such that

$$\big((U^n - U^{n-1})k_n^{-1} + (\bar{U}^n \cdot \nabla)\bar{U}^n, v\big) + \big(2\vartheta\epsilon(\bar{U}^n), \epsilon(v)\big) - (P^n, \nabla \cdot v) + (\nabla \cdot \bar{U}^n, q) + SD_\delta^n(\bar{U}^n, P^n; v, q) = (f, v)$$

$$\forall \hat{v} = (v, q) \in V_0^n \times V_h$$

Where: $\bar{U}^n = 1/2(U^n + U^{n-1})$ is piecewise constant in time over I_n , with the stabilizing term,

$$SD_\delta^n(\bar{U}^n, P^n; v, q) \equiv (\delta_1(\bar{U}^n \cdot \nabla \bar{U}^n + \nabla P^n - f), \bar{U}^n \cdot \nabla v + \nabla q) + (\delta_2 \nabla \cdot \bar{U}^n, \nabla \cdot v)$$

..... (ii)

Where we have dropped the shock capturing term and where

$$(v, w) = \sum_{k \epsilon T_n} \int_k (v \cdot w \, dx)$$

$$\big(\epsilon(v), \epsilon(w)\big) = \sum_{i,j=1}^{3} \Big(\epsilon_{ij}(v), \epsilon_{ij}(w)\Big)$$

with the stabilization parameters

$$\delta_1 = k_1(k_n^{-2} + |U^{n-1}|^2 h_n^{-2})^{-\frac{1}{2}}$$

$$\delta_2 = k_2 h_n$$

where k_1 and k_2 are positive constants of unit size.

For turbulent flow, the time step size is

$$k_n \sim \min_{x \in \Omega} \left(\frac{h_n}{|U^{n-1}|} \right)$$

The least squares stabilization omits the time derivative in the residual, which is a consequence of the test functions being piecewise constant in time for $cG(1)$discretization of time.

4.4. Software Environment

The software environment shows the interdepencencey of each software at different stages of the simulations.

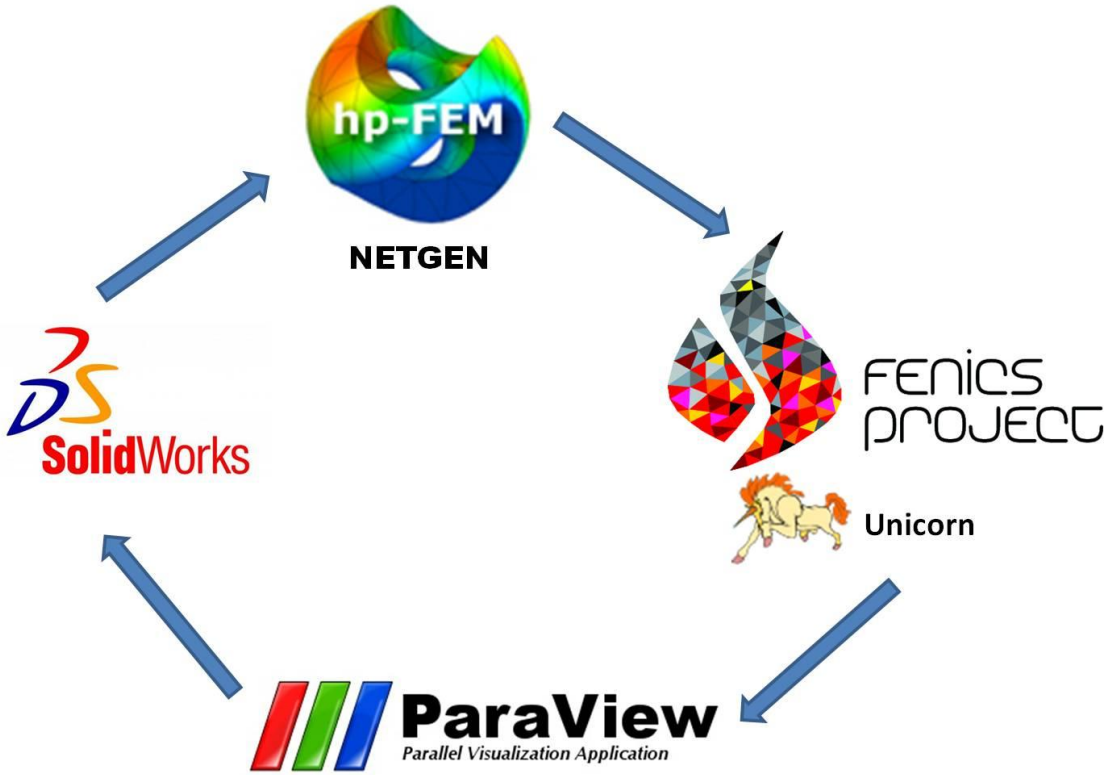

Figure 14 : Overview of the Software Environment

SolidWorks

The SolidWorks® CAD software is a mechanical design automation application that lets designers quickly sketch out ideas, experiment with features and dimensions, and produce models and detailed drawings.

NETGEN

NETGEN is an automatic 3d tetrahedral mesh generator. It accepts input from constructive solid geometry (CSG) or boundary representation (BRep) from STL file format. The connection to a geometry kernel allows the handling of IGES and STEP files. NETGEN contains modules for mesh optimization and hierarchical mesh refinement. Netgen is open source based on the LGPL license. It is available for Unix/Linux and Windows.

Unicorn

Unicorn is a massively parallel adaptive finite element solver technology. Unicorn aims at developing one unified continuum mechanics solver for a wide range of applications, based on the suite DOLFIN/FFC/FIAT.

ParaView

ParaView is an open-source, multi-platform data analysis and visualization application. ParaView users can quickly build visualizations to analyze their data using qualitative and quantitative techniques. The data exploration can be done interactively in 3D or programmatically using ParaView's batch processing capabilities.

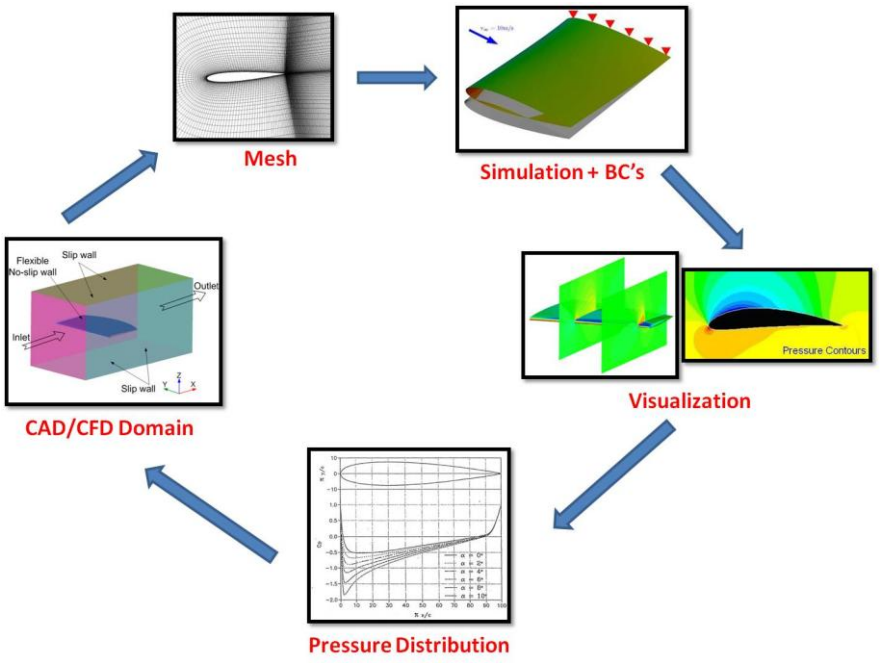

Figure 15 : Software correlations at each stage

4.5. Geometry Modelling

The CAD model of the NACA 64(2)-415 section airfoil with 242 mm chord and 1200 mm span were generated as the dimensions relative to the prototype. The 3D wing model and the computational domain is generated by using SolidWorks® CAD software [19].

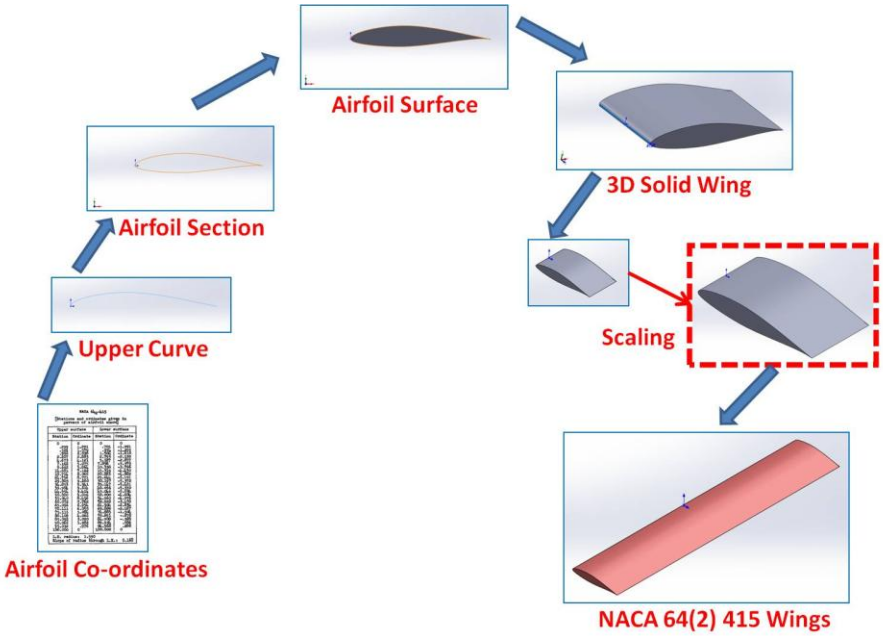

Figure 16 : 3D CAD modelling of the NACA Wing

Two variants were considered for the investigation ”clean wing” and ”protrusion wing”. Clean wing is the standard wing and the protrusion wing is standard wing with a geometry modification (semi circular boss near the leading egde). The semi-circular protrusion is located at the 8% of the chord length.

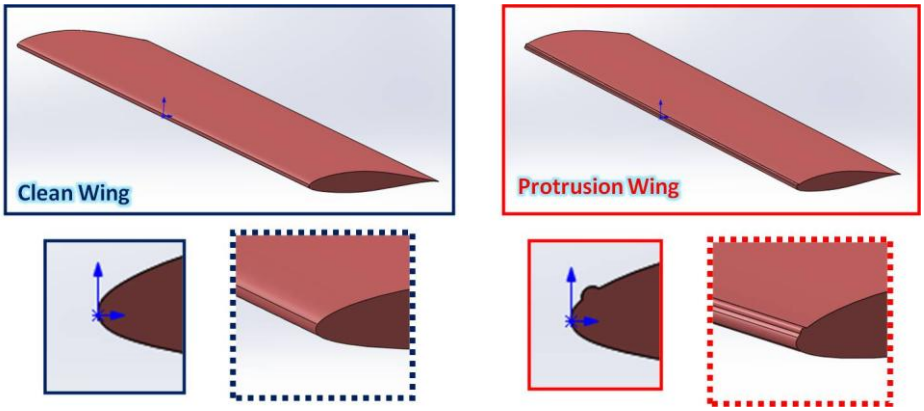

Figure 17 : Clean Wing and Protruson Wing CAD Models

A benchmark study was executed to decide the location of the protrusion for the protrusion wing. Three models were considered for the study. Simulations were computed for an angle of attack (AOA) = 10,

Model 1 – Clean wing

Model 2 – Protrusion @ 4% of the chord from the leading edge

Model 3 – Protrusion @ 8% of the chord from the leading edge

Numerical Results comparison:

From the comparative study and the visualization plots, Model 3 with protrusion at 8% of the chord has a significant effect on the drag coefficient and lift coefficient. Hence "Model 3 with protrusion at 8% of chord" was chosen for our project.

Models	Lift Coefficient [Cl]	Drag Coefficient [Cd]
Model 1	1.445	0.0389
Model 2	1.395	0.0581
Model 3	1.316	0.1251

Velocity Magnitude Plots

Model 1 Model 2 Model 3

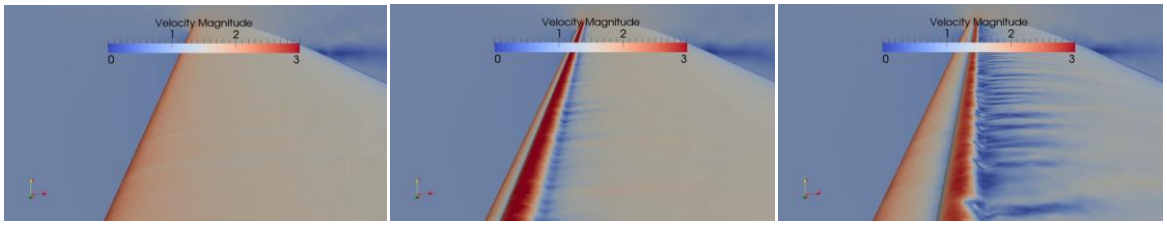

Figure 18 : Comparison of the velocity magnitude over the leading edge

Pressure Plots

Model 1 Model 2 Model 3

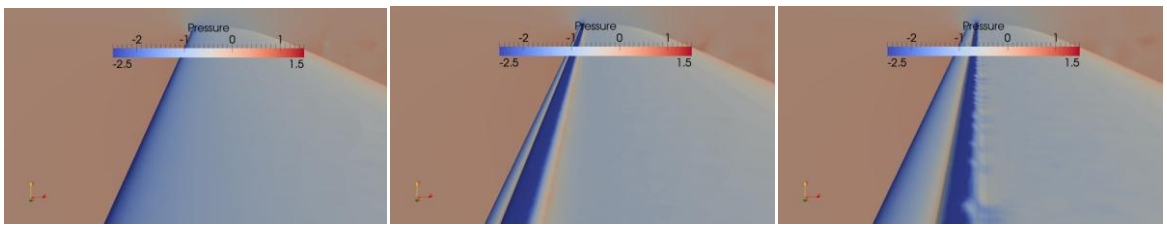

Figure 19 : Comparison of the pressure distribution over the leading edge

4.6. Mesh Generation

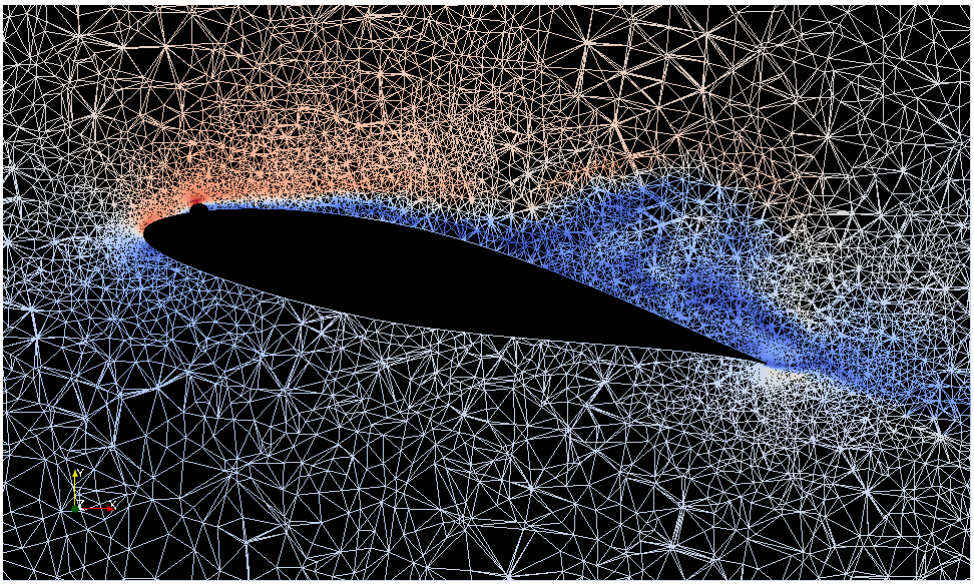

Figure 20 : Tetrahedral mesh for the Protrusion Wing model

An Unstructured grid of tetrahedral mesh is used for the entire solution domain. Mesh generation is done in “NETGEN”. After mesh has generated, the mesh is saved in “.gmsh” file format and converted to “.xml” format as an input to the Unicorn.

Mesh Dependency

Mesh dependency was investigated at “angle of attack 6” for both clean wing and protrusion wing. The study of two sensitive parameters “coefficient of LIFT “and “coefficient of DRAG” were carried out.

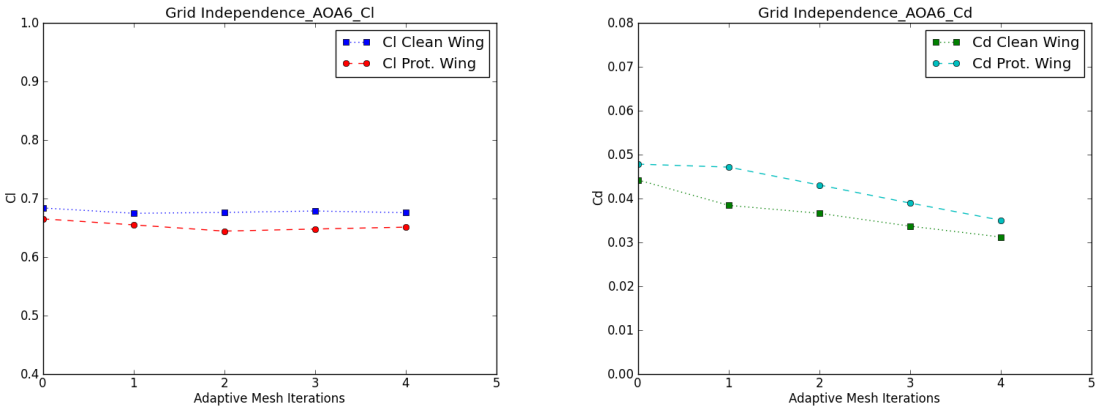

Figure 21 : Grid Dependency Cl and Cd vs. Adaptive mesh refinements

From fig – 19, it can be observed that the coefficient of lift doesn't vary with increasing the mesh refinements. In case of coefficient of lift, the trend is approaching for an average value with cumulative difference of 1.5%. Where as in case of coefficient of drag, the trend is still following a downward path indicating we would need some more mesh refinement before we can state mesh convergence for drag.

In order the study effect of refinement, cumulative data **[% Δ Cd]c** and **[% Δ Cd]c** was extracted for coefficient of lift and drag.

Data for Clean Wing, AOA = 6					
Iterations	**Mesh Nodes**	**Cl**	**Cd**	**[% Δ Cl]c**	**[% Δ Cd]c**
0	236960	0.6838	0.0442	NA	NA
1	375277	0.6747	0.0384	1.3	13.1
2	526301	0.6761	0.0366	-0.2	4.7
3	733875	0.6787	0.0337	-0.4	8.0
4	1019839	0.6757	0.0312	0.4	7.3

Data for Protrusion Wing, AOA = 6					
Iterations	**Mesh Nodes**	**Cl**	**Cd**	**[% Δ Cl]c**	**[% Δ Cd]c**
0	302296	0.6651	0.0478	NA	NA
1	461643	0.6549	0.0471	1.5	1.4
2	627829	0.6443	0.0430	1.6	8.7
3	866578	0.6478	0.03895	-0.5	9.5
4	1198531	0.6511	0.0350	0.5	10.0

4.7. Boundary Conditions for the Computational Domain

For Incompressible flow problems, ”Velocity inlet and Outflow BC’s” are a recommended. Use of ”pressure outlet” instead of outflow often results in better rate of convergence when backflow occurs.

The following boundary conditions were adopted for our case: velocity inlet, pressure outlet and slip walls. The magnitude of velocity is 20 m/s in the experimental investigations.

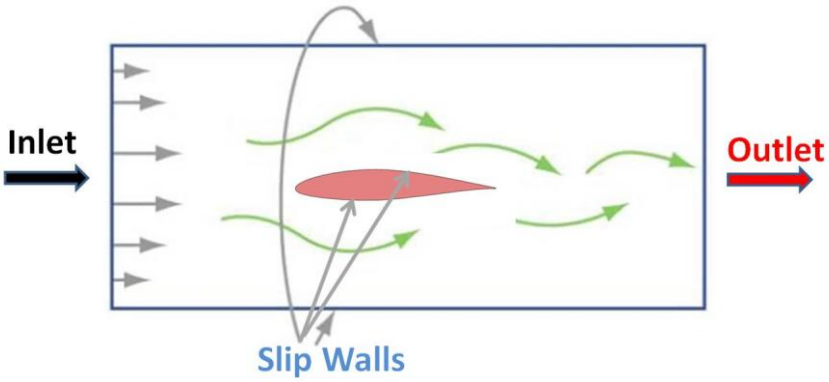

Figure 22 : Boundary conditions for flow around an Airfoil

4.8 Solving

The numerical investigations were executed with the massively parallel unified continuum adaptive finite element method solver “Unicorn” and the computing resources at KTH – CTL. Simulations were computed on the Lindgren Cray XE6 super computer using 100 – 400 cores. The solving time for each iteration is about 6-8 hours for the finer mesh of 1198531 nodes [2000 core hours].

4.9 Results

We have considered clean wing and the protrusion wing for the plots for AOA = 6, 12 and 20. Post-Processing of the results were carried out in ”Paraview” and the following plots were extracted :

1. Mesh Plots
2. Pressure plots
3. Velocity Plots
4. Velocity Vorticity Plots

Mesh Plots

Three dimensional unstructured tetrahedral meshes were generated using an adaptive mesh algorithm.The mesh distribution over the wings are visualized in Paraview. From the following mesh plots we can observe that finer mesh are around boundary of the airfoil and coarse meshes are in the outer region.

AOA = 6

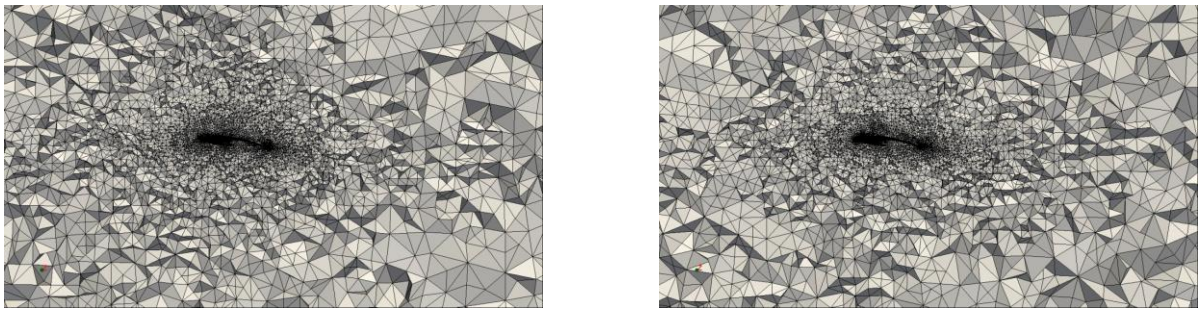

AOA = 12

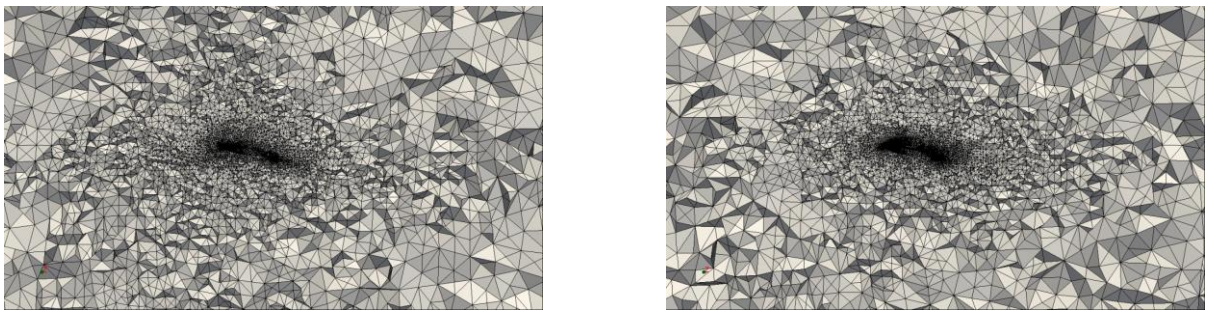

AOA = 20

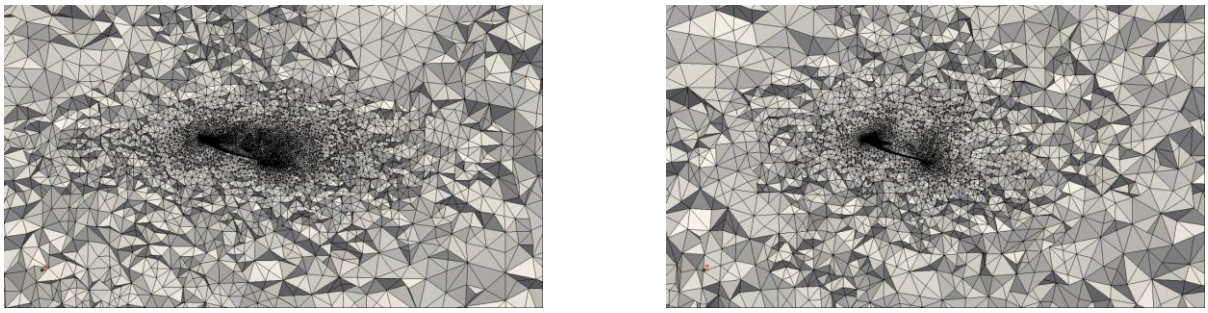

Figure 23 : Mesh plots at different AOA for Clean (Left) and Protrusion Wing (Right)

2D Pressure Plots

Fig. 24 shows the comparison of the pressure distribution for clean wing and protrusion wing for angle of attacks (AOA) 6, 12 and 20.

AOA = 06

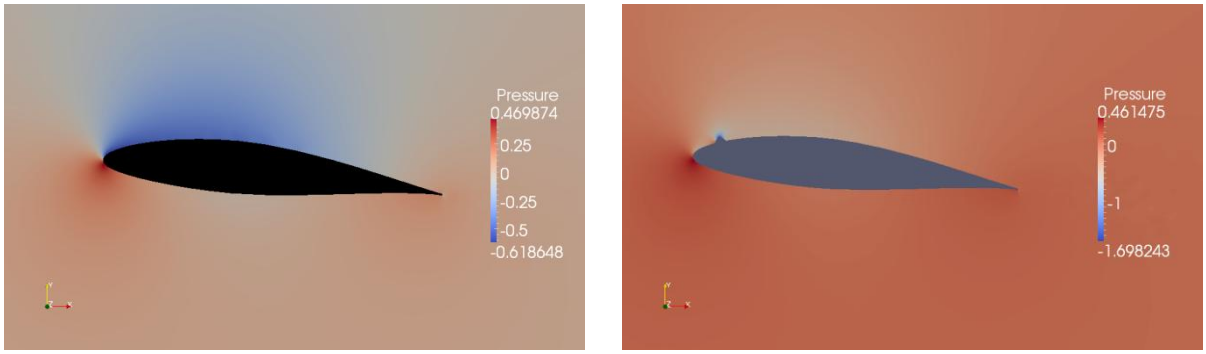

AOA = 12

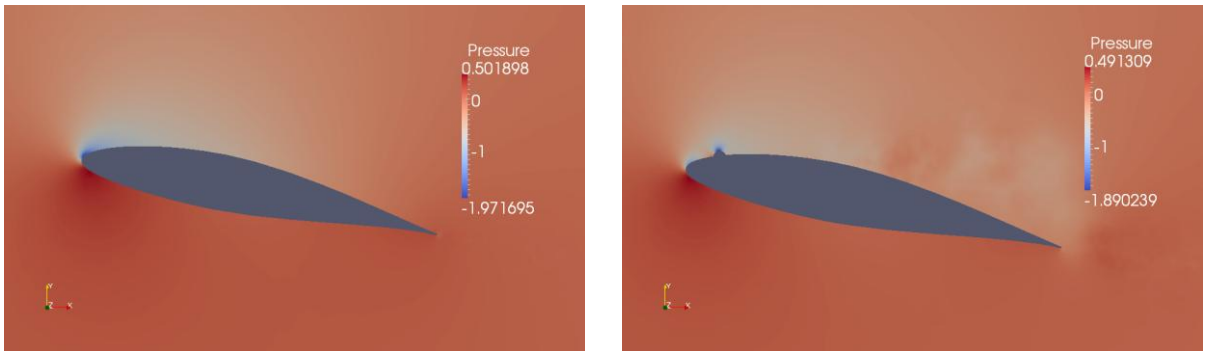

AOA = 20

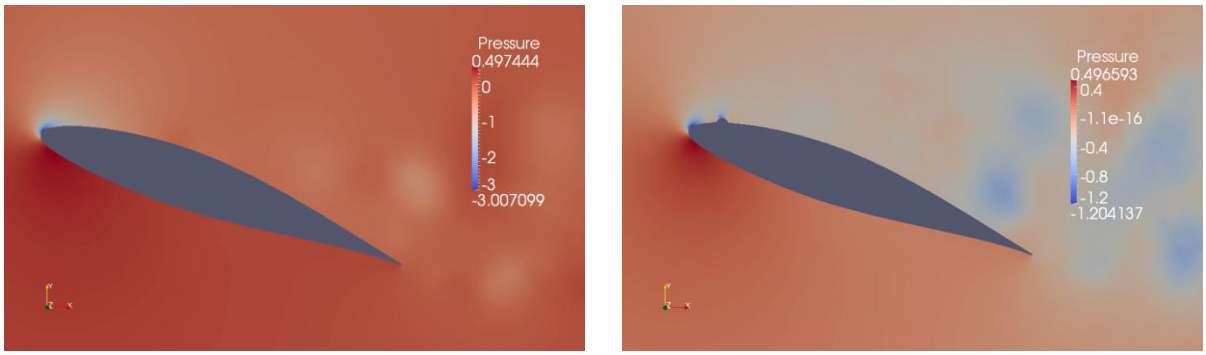

Figure 24 : 2D Pressure plots at different AOA for Clean wing (Left) and Protrusion Wing (Right)

2D Velocity Plots

Fig. 25 shows the comparison of the velocity magnitude for clean wing and protrusion wing for angle of attacks (AOA) 6, 12 and 20. From the velocity plots, It can observed that protruison wing is more prone to flow separation as compared to the clean wing at angle of attack 12 and 20.

AOA = 06

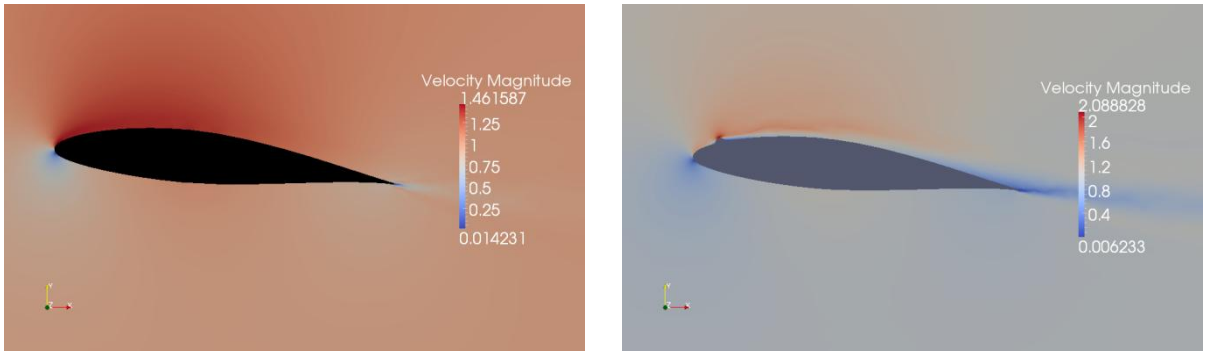

AOA = 12

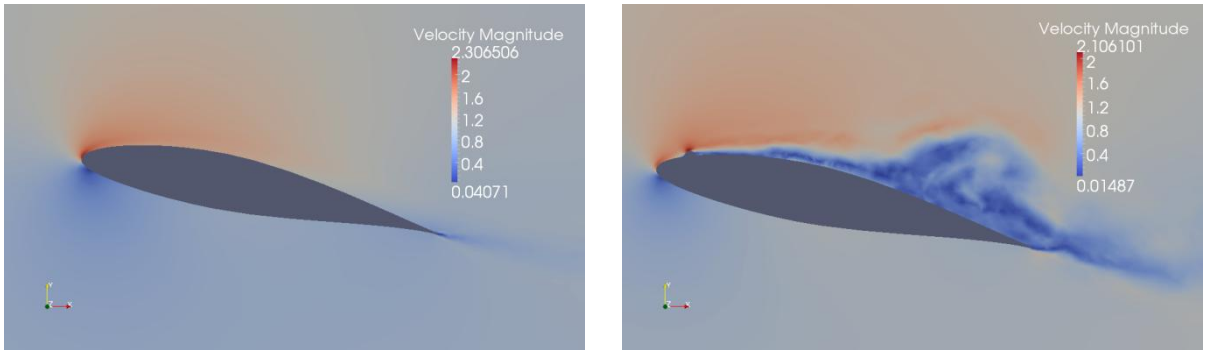

AOA = 20

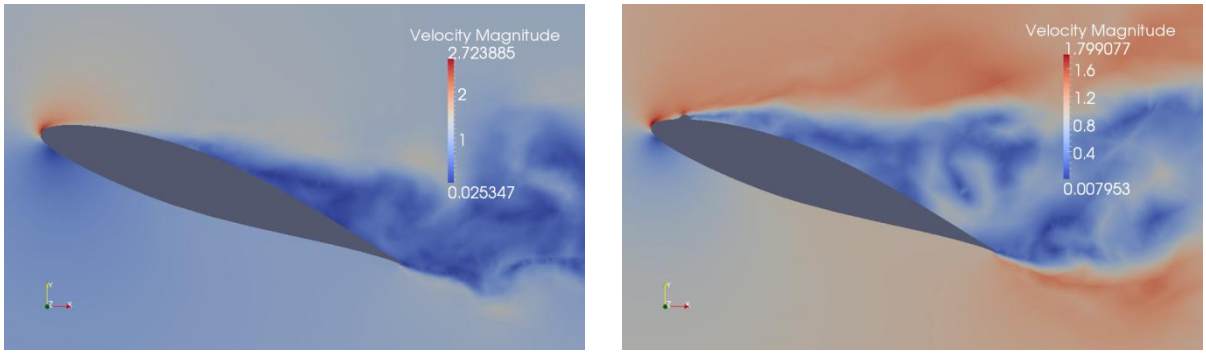

Figure 25 : 2D Velocity plots at different AOA for Clean wing (Left) and Protrusion Wing (Right)

3D surface Pressure and Velocity Plots

Fig. 26 shows the comparison of the pressure and velocity distribution over the 3D wing. Clean wing and protrusion wing were mereged for a clear visualization of the pressure and velocity distribution. It can observed that a significant effect of geometry modification on the pressure and velocity distribution. As the angle of attack increases the maximum velocity magnitude of the turbulent flow increases .

AOA = 6

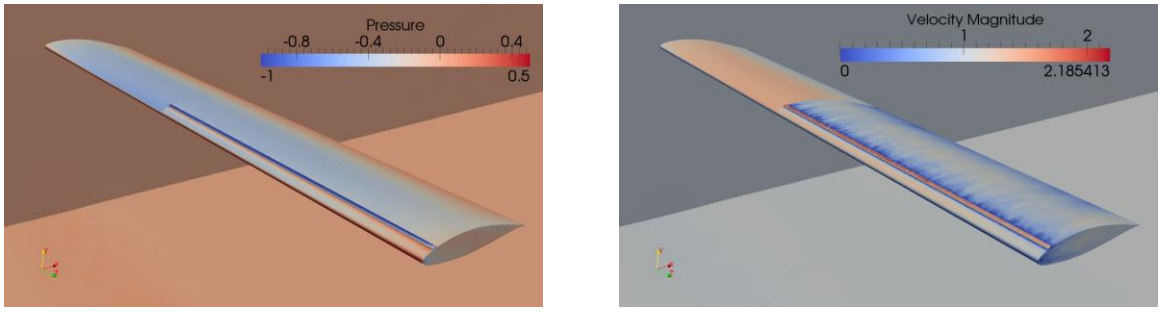

AOA = 12

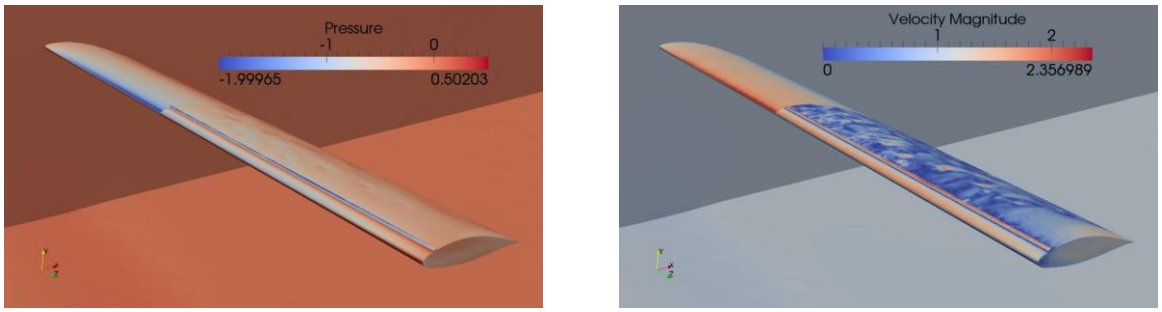

AOA = 20

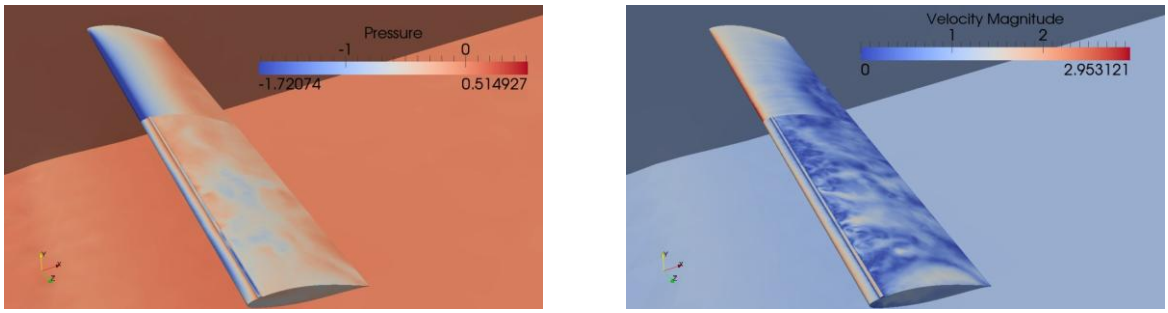

Figure 26 : Pressure and Velocity distribution at different AOA for Clean (Left half) and Protrusion Wing (Right half)

Velocity Vorticity Plots

The velocity vorticity plots over the wings are one critical parameter to study in a aerodynamic simulations. From the following plots we can observe that protrusion wing model has higher tendency for the vorticities as compared to the clean wing.

AOA = 6

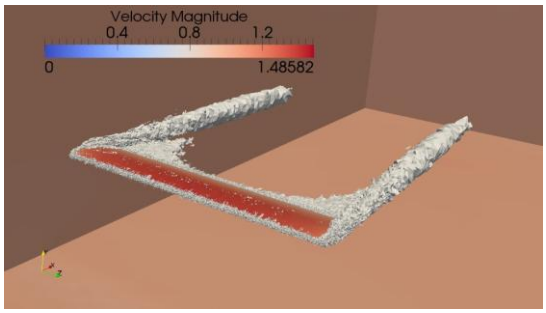

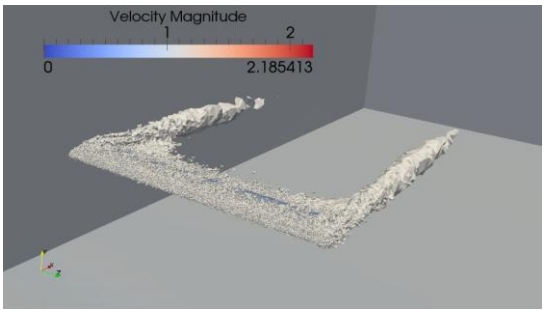

AOA = 12

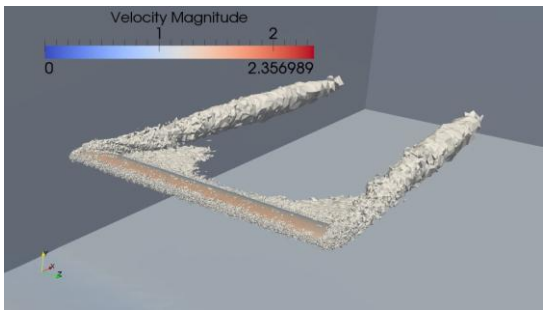

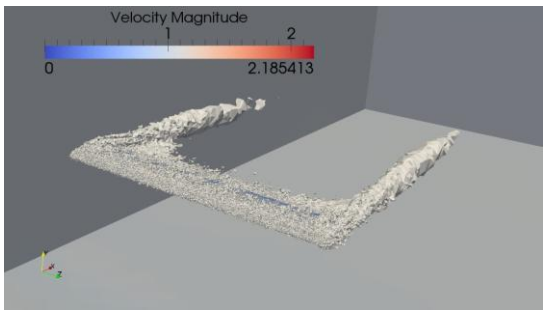

AOA = 20

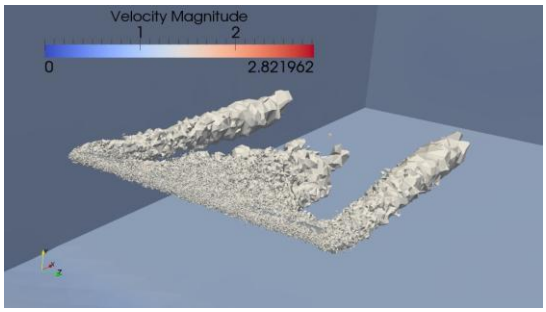

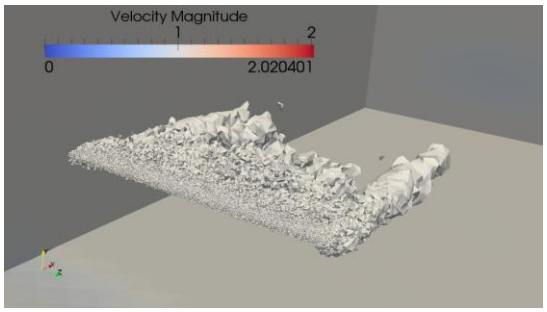

Figure 27 : Velocity Vorticity plots at different AOA for Clean (Left) and Protrusion Wing (Right)

5. Experimental Investigation

5.1. Description of the Experimental Setup

Experiments were carried out in the low speed wind tunnel of the Norwegian University of Science and Technology (NTNU), Trondheim.

Figure 28 : NTNU's Wind Tunnel

The wind tunnel is a closed-return wind-tunnel that is principally used for three-dimensional testing. A heat exchanger, honeycomb and three turbulence reduction screens are located at the inlet settling chamber. The test section dimensions are 2.7m x 1.8m x 11m and maximum velocity of 30 m/s. Desired airspeed is achieved using a variable frequency drive. Fig. 27 shows a picture of the wind tunnel facilities.

The wing prototype used for this investigation was NACA 64(2)-415 airfoil with 0.242m in chord, 1.2m in span, and was mounted horizontally in the test section. The prototype is made from wood with synthetic coating. Two design variants *"clean wing model"* and the *"protrusion wing model"* were used for the experiments. Protrusion variant was developed by nailing a semi-spherical wooden strap at 8% of the chord from the leading edge.

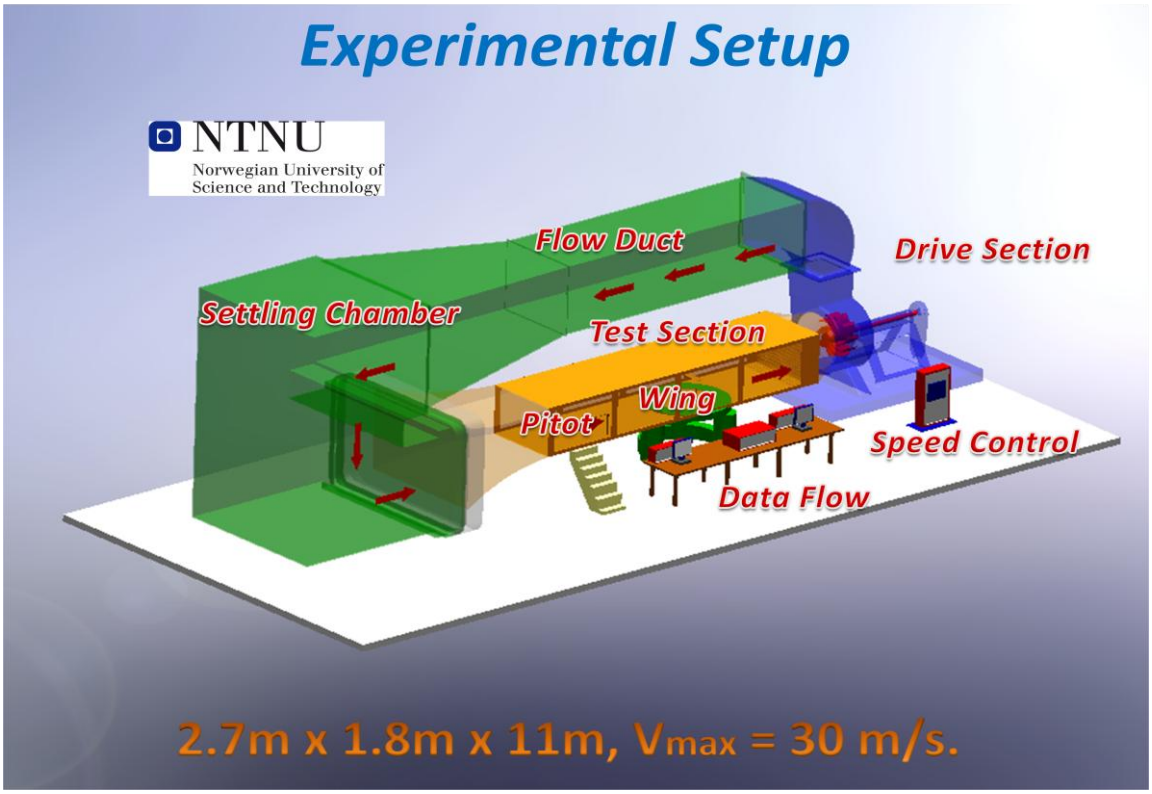

Figure 29 : : NTNU's Wind Tunnel Set-up

5.2. Measurements

A high resolution 6 component electronic wind tunnel balance is used for the velocity – pressure - force measurements. A large number of high speed 12 bit data acquisition with signal conditioning amplifiers and filters are available capable of recording data continuously to disk at a rate up to 1 MHz.

5.2.1 6-Loaded Cell Measurements:

It's a 6 loaded cell which is used to measure the vertical and horizontal forces. The Measurements are in "Newton (N)" which is converted into "Voltage (v)" by an AC/DC converter.

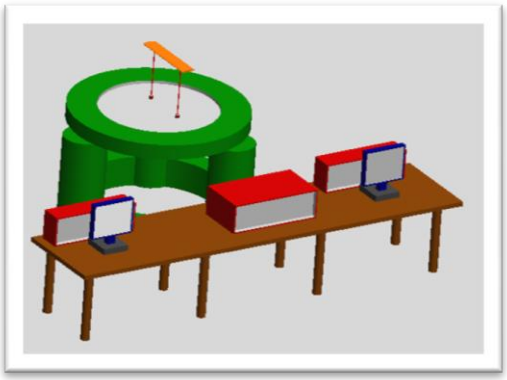

Figure 30 : 6 loaded cell unit

5.2. 2 Pressure Measurements :

Static and Dynamic pressure are measured at the wing surface and at the pitot tube with a pressure transducer.

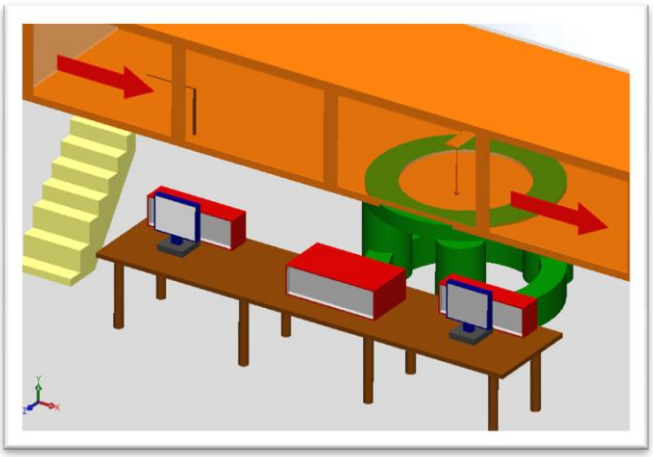

Figure 31 : Pressure Measurement Units

Pressure taps were mounted on the upper and lower surfaces of the wing. The pressure taps are connected to the pressure inducer and the measuring units.

Figure 32 : Pressure Transducer and Data flow of from the Pressure Taps on the wing

5.2. 3 Angle of Attack [AOA] Measurement

Angle measurements were carried out manually with a digital protractor and a custom made level made from wood.

Figure 33 : Tools for the Angle of Attack Measurements

5.2. 4 TUFTS Visualization

TUFTS visualization is carried out by attaching 50 - 60 thread TUFTS of four rows on to the upper surface of the wing model. When the wind is turned on the tufts move in the direction of the flow. Flow visulaizations were carried out for number of angles from stagnation still stall.

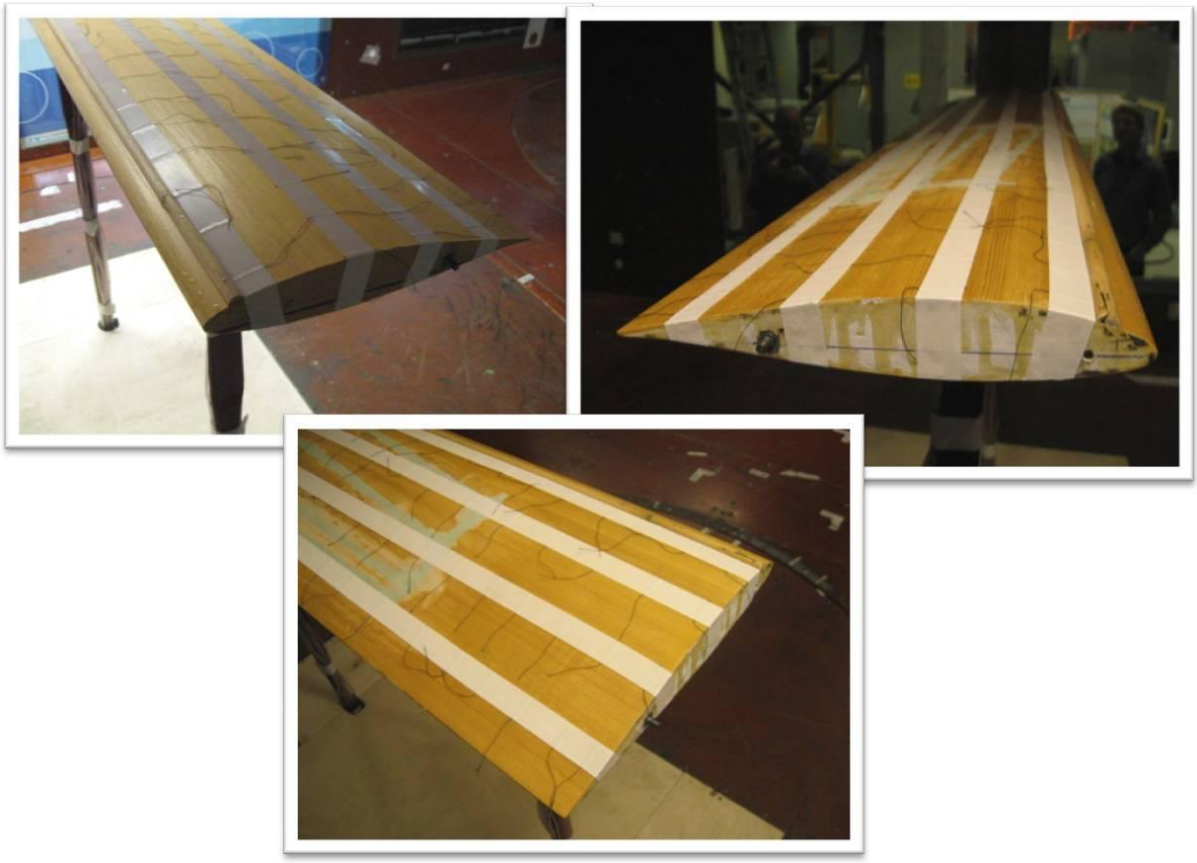

Figure 34 : Threaded TUFT Visualization of the Protrusion Wing Model

6. Results Comparison and Discussion

The aerodynamic performance characteristics of the NACA 64(2)-415 wing are presented for the two design variants ”clean wing” and the ”protrusion wing”. The experimental and numerical solutions were compared to investigate the effect of the geometry modification on the aerodynamic characteristics and to measure the deviation.

Description	Reynolds Number	Wing Tip
NTNU Experiment (3D)	3.2×10^5	Filleted Wing tip edges
NACA Experiment (2D)	3.1×10^6	Free wing tip
Numerical Simulation (3D)	Higher ($\approx \infty$)	Filleted Wing tip edges

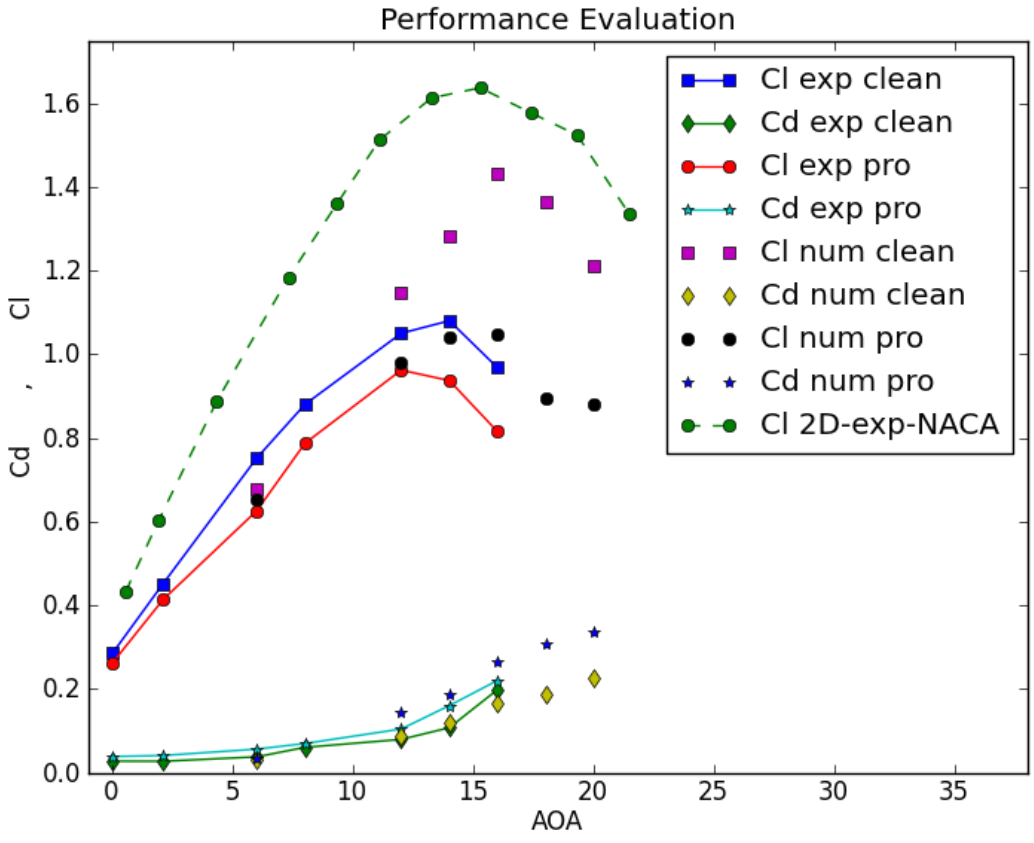

Figure 35 : Performance Evaluation

As can be seen in Fig.35 the geometry modification has a significant effect on the aerodynamic characteristics such as coefficient of lift, coefficient of drag and stall conditions of the NACA 64(2)-415 wing model. Stall conditions and coefficient of lift are the key parameters for our investigation. As stall angles are sensitive with respect to reynolds number, reference 2D NACA experimental values were also considered [17] for the evaluation.

	Clean Wing		*Protrusion Wing*	
	Expt.	**CFD**	**Expt.**	**CFD**
Stall Angle Range	13.5 – 14.5	16.0 – 17.0	11.5 – 12.5	14.0 – 16.0
Maximun cl - AOA	14	16	12	14

The deviation of the experimental results and the numerical results were extracted in terms of the percentage deviation of "**cl"** and "**cd**" for both clean wing and protrusion wing.

Experiment vs. Numerical				
	Clean Wing		Protrusion Wing	
AOA	**Δ%cl**	**Δ %cd**	**Δ %cl**	**Δ %cd**
6	9.7	20.7	-0.9	32.1
12	-9.3	-9.4	-2.4	-39.2
14	-18.8	-18.6	-11.7	-17.1
16	-48.2	15.7	-23.2	-19.9

The percentage deviation of coefficient of lift **(Cl)** and coefficient of drag **(Cd)** for both clean wing and protrusion wing are :

Experimental Results						
	Clean Wing		**Protrusion Wing**		**% Deviation (Δ)**	
AOA	**Cl**	**Cd**	**Cl**	**Cd**	**Δ %Cl**	**Δ %Cd**
06	0.752178	0.037417	0.625919	0.055894	16.8	-49.4
12	1.047963	0.079118	0.962177	0.104040	08.2	-31.5
14	1.079983	0.101715	0.936957	0.159944	13.2	-57.2
16	0.968130	0.198177	0.815094	0.219583	15.8	-10.8

Numerical Results						
	Clean Wing		**Protrusion Wing**		**% Deviation (Δ)**	
AOA	**Cl**	**Cd**	**Cl**	**Cd**	**Δ %Cl**	**Δ %Cd**
06	0.679338	0.029659	0.631328	0.037924	07.1	-27.9
12	1.145383	0.086543	0.984978	0.144825	14.0	-67.3
14	1.283091	0.120631	1.046267	0.187225	18.5	-55.2
16	1.435059	0.167134	1.004376	0.263374	30.0	-57.6

7. Conclusions

The experimental and numerical investigations have been performed for two cases (Clean wing and Protrusion wing) of the NACA 64(2)415 wing. The numerical investigation was executed with the massively parallel unified continuum adaptive finite element method solver ”Unicorn”. The accuracy of the numerical results has been validated against the experimental results. The results comparison show that the deviation between the experimental and numerical results is small for the lower angles of attack and gradually increases for higher angles of attack. The study also shows that the protrusion wing resulted in a lower lift and higher drag as compared to the clean wing.

Our investigation leads to the following conclusions :

1. The experimental and numerical results have good correlations for lower range of angle of attack *(6°–12°)* before stall angle. The average percentage difference compared to experiment is less than 10 % for coefficient of lift and less than 30 % for coefficient of drag. The errors are within the acceptable range, compared to the previous research [6, 13] which is a positive outcome of the project.

2. The percentage difference after the stall angle is large. The main reason for this large difference in the clean wing is due to the difference in the reynolds number(Re) , which in turn has a large effect on the stall angle. The reynolds number considered for experiment investigation is $\approx 10^5$, where as for numerical investigations Re is considered to be high $(Re \approx \infty \; or \; Viscosity = 0)$.

3. The numerical results of the clean wing have a close relevance with the reference NACA published results. Especially the stall angle for the clean wing and reference NACA values are in a range of 16°–*17*°. From the reference

NACA published results we can conclude that stall angles are sensitive to the reynolds number(Re).

4. Protrusion wing model resulted in lower lift, higher drag and earlier stall as compared to the clean wing model. The average percentage reduction in lift is ca. 15 % and increase in drag 40 – 50 %, both in experiments and simulations.

5. From the mesh convergence study, we can summarize that the average percentage variation of coefficient of lift is less than 5 % with respect to the last 5 adaptive iterations. The results comparison was done with the consecutive adaptive mesh iterations.

6. Additional experimental investigations for the new designs would leads to additional cost, so in this scenario numerical simulations would be a cost effective solution.

8. Scope for future work

Our research and results presented in this thesis provide valuable insight to understand the effect of geometry modification on the aerodynamic characteristics of a wing and overview of Unicorn framework .

The following scope for future work were identified :

1. To get a better understanding of the effect of protrusion an in-depth pressure distribution study over the Clean and Protrusion wings are required.
2. In order to expand the horizon of the project, numerical investigations for “Dented” and “Leading Edge Tubercles” case studies would be a new area of interest.

9. References

[1] P. Moin, J. Kim, Tackling turbulence with supercomputers, Scientific American, 1997.

[2] P. Moin, D. You, Active control of flow separation over an airfoil using synthetic jets, Journal of Fluids and Structures 24, 2008

[3] P. Sagaut, Large Eddy Simulation for Incompressible Flows (3rd Ed.), Springer-Verlag, Berlin, Heidelberg, New York, 2005

[4] J. Hoffman, C. Johnson, Computational Turbulent Incompressible Flow, Vol. 4 of Applied Mathematics: Body and Soul, Springer, 2007.

[5] J. Hoffman, J. Jansson, C. Degirmenci, N. Jansson, M. Nazarov, Unicorn: A Unified Continuum Mechanics Solver, in: Automated Scientific Computing, Springer, 2011

[6] J. Hoffman, Computation of mean drag for bluff body problems using adaptive dns/les, SIAM J. Sci. Comput. 27(1) (2005) 184–207

[7] J. Hoffman, J. Jansson, C. Degirmenci, N. Jansson, M. Nazarov, Unicorn: A Unified Continuum Mechanics Solver, in: Automated Scientific Computing, Springer, 2011

[8] J. Hoffman, Adaptive simulation of the subcritical flow past a sphere, J. Fluid Mech. 568 (2006) 77–88.

[9] J. Hoffman, Efficient computation of mean drag for the subcritical flow past a circular cylinder using general Galerkin G2, Int. J. Numer. Meth. Fl. 59 (11) (2009) 1241–1258

[10] J. Hoffman, N. Jansson, A computational study of turbulent flow separation for a circular cylinder using skin friction boundary conditions, in: Quality and Reliability of Large-Eddy Simulations II, Vol. 16 of ERCOFTAC Series, Springer Netherlands, 2011, pp. 57–68

[11] R. V. de Abreu, N. Jansson, J. Hoffman, Adaptive computation of aeroacoustic sources for rudimentary landing gear, in: proceedings for Benchmark problems for Airframe Noise Computations I, Stockholm, 2010.

[12] N. Jansson, J. Hoffman, M. Nazarov, Adaptive Simulation of Turbulent Flow Past a Full Car Model, in: Proceedings of the 2011 ACM/IEEE

[13] Johan Hoffman, Johan Jansson, Niclas Jansson, *Simulation of 3D unsteady incompressible flow past a NACA 0012 wing section*, Computational Technology Laboratory, CSC/NA, KTH, 2012.

[14] J. Hoffman and C. Johnson, *Computational Turbulent Incompressible Flow,* Springer 2007.

[15] Hoffman J, Jansson J, Nazarov M, Jansson N, *Unicorn 2011* ,http://launchpad.net/unicorn/hpc.

[16] Laurence K. Loftin Jr., M Irene Poteat, *Aerodynamic Characteristics of several NACA airfoil sections at seven Reynolds number from 0.7x10^6 to 9.0x10^6*, Langley Memorial Aeronautical Laboratory, 1948.

[17] Ira H. Abbott, Albert E. Von Doenhoff ,and Louis S Stivers Jr, Summary of Airfoil Data, 1945.

[18] Johan Jansson, Course modules for "DN2260 The Finite Element Method", KTH, 2012

TRITA-MAT-E 2013:11
ISRN-KTH/MAT/E--13/11-SE

www.kth.se